

Freezing of Fluids Confined between Mica Surfaces

K. G. Ayappa* and Ratan K. Mishra

Department of Chemical Engineering, Indian Institute of Science, Bangalore 560012, India

Received: April 13, 2007; In Final Form: August 29, 2007

Using grand ensemble simulations, we show that octamethylcyclotetrasiloxane (OMCTS) confined between two mica surfaces can form a variety of frozen phases which undergo solid–solid transitions as a function of the separation between the surfaces. For atomically smooth mica surfaces, the following sequence of transitions $1\Delta \rightarrow 1\Delta_b \rightarrow 2B \rightarrow 2\Box \rightarrow 2\Delta$ are observed in the one- and two-layered regimes, where $n\Delta$, $n\Box$, and nB denote triangular, square, and buckled phases, respectively, with the prefix n denoting the number of confined layers. The presence of potassium on mica is seen to have a strong influence on the degree of order induced in the fluid. The sequence of solid–solid transitions that occurs with the smooth mica surface is no longer observed. When equilibrated with a state point near the liquid–solid transition, a counterintuitive freezing scenario is observed in the presence of potassium. Potassium disrupts in-plane ordering in the fluid in contact with the mica surface, and freezing is observed only in the inner confined layers. The largest mica separations at which frozen phases were observed ranged from separations that could accommodate six to seven fluid layers. The extent of freezing and the square-to-triangular lattice transition was found to be sensitive to the presence of potassium as well as the thermodynamic conditions of the bulk fluid. The implications of our results on interpretation of surface force experiments as well as the generic phase behavior of confined soft spheres is discussed.

1. Introduction

Soft sphere fluids confined to a few atomic layers can crystallize and undergo solid–solid transformations between n square (\Box) and n triangular (Δ) lattices, where n is the integral number of layers in the pore. The phenomenon of fluid layering and the accompanying oscillatory force response when a fluid is confined between two surfaces has been well-documented.^{1–5} Epitaxial freezing occurs when the symmetry of the confined phase is determined by the atomic structure of the confining surface.^{6,7} In the absence of epitaxial freezing, a sequence of transitions between square and triangular symmetry has been recently investigated for confined soft spheres.^{8–11} This sequence of solid–solid transitions has been experimentally observed for colloidal suspensions confined between glass plates^{12–14} and studied using simulations of confined hard spheres.^{15–19} In addition to triangular and square lattices, buckled and prism phases which have been observed in experiments with colloids²⁰ are also shown to be thermodynamically stable.²¹ The studies on confined soft spheres illustrate the generic nature of these confinement driven transitions which occur over length scales spanning the colloidal regime down to atomic dimensions.

Grand canonical Monte Carlo (GCMC) simulations with fluids interacting with a 12–6 Lennard-Jones potential have shown the presence of a $2\Box$ -to- 2Δ transition for xenon confined between two structured surfaces.⁸ Investigation of methane confined in graphitic pores revealed a rich sequence of solid–solid transformations between $n\Delta$ to $(n + 1)\Box$ phases extending up to $n = 4$.^{9,22} The 1Δ structure transforms to the $2\Box$ structure through an intermediate random buckled phase. Splitting in the solvation force peaks at a fixed number of fluid layers in the region where a transition from $n\Box$ to $n\Delta$ symmetry is observed, which is seen as a distinct signature of the change in lattice structure.^{8,9,22} Solid–solid transformations from $n\Box$ to $n\Delta$ (n

= 1, 2, 3) phases have also been reported in freezing studies by Vishnyakov and Neimark¹⁰ for nitrogen in graphitic pores. This study reveals a non-monotonic dependence of freezing temperature on surface separation, with the $2\Box$ structures freezing at lower temperatures than the 1Δ and 2Δ structures. The study also locates the presence of a quadratic phase characterized by an algebraic decay of the bond-orientational correlation functions. Transitions in stacking symmetry for the 3Δ phase from ABA to ABC have also been observed with increasing surface separation.^{9,10} Molecular dynamics simulations in a wedge shaped pore with a truncated and shifted Lennard-Jones potential illustrate a transition within a bilayer from square to triangular symmetry at small wedge angles.²³

The templating effect of pore wall lattice structures on the transformation between lattices of square and triangular symmetry for Lennard-Jones fluids have also been investigated.^{11,24,25} When bilayers are confined between walls consisting of a lattice with square symmetry,¹¹ epitaxial $2\Box$ structures are observed at the smaller surface separations, transforming to the 2Δ phase as the separation is increased. Increasing the strength of the fluid–wall interaction is seen to increase the range of temperatures and surface separations over which the epitaxial phases are stable. The presence of domain walls has also been observed in the epitaxially frozen structures.¹¹ Phase diagrams for pores which accommodate three to five layers²⁴ indicate that the surface separation has a stronger influence on the fluid structure when compared with the effect of the fluid–wall interaction strength. In all cases, stacking sequences corresponding to the ABA sequence were observed.²⁴

Lattice based density functional theories have also been used to study the sequence of solid–solid transformations for confined soft sphere systems.^{26,27} The zero temperature lattice model by Bock et al.²⁷ reveals the presence of a stable line buckled phase in the transition from one to two fluid layers, and the overall predictions of the transitions between square and triangular symmetry are in good agreement with previous

* Corresponding author. E-mail: ayappa@chemeng.iisc.ernet.in. Fax: 011-91-80-3600683 (3600085).

GCMC simulations for the same system. On the basis of the packing geometries of various solid structures, the high pressure adsorption capacities were found to agree well with simulation data.²⁶

Free energy computations using the Landau–Ginzburg method have been used to study the phase behavior of confined fluids.^{28–31} The strength of the fluid–wall interaction strength is found to have a strong influence on the freezing temperature (relative to the bulk) of the confined fluid. In pores with strong fluid–wall interactions such as mica and carbons, the freezing temperature is elevated with respect to the bulk, and for weakly interacting pores, the freezing temperature is depressed relative to the bulk. On the basis of a dimensionless analysis, the elevation or depression for fluids with weak to moderate fluid–fluid interactions is found to depend on the reduced surface separation, $H^* = H/\sigma_{ff}$ (where σ_{ff} is the fluid–fluid diameter in the Lennard-Jones potential), and a dimensionless parameter, α , which depends on the density of atoms in the pore wall, the ratio of the fluid–fluid and fluid–wall interaction energies, and the interlayer spacing of wall atoms that comprise the pore wall. Simulations carried out for a wide variety of systems in smooth walled pores for Lennard-Jones fluids reveal an elevation in freezing temperature for $\alpha > 1.15$ and a depression in freezing temperature for $\alpha < 1.15$. Under certain conditions, a stable hexatic phase is observed between the confined liquid and frozen phases. These findings on the elevation and depression of melting temperatures are in agreement with experiments on similar systems.³¹

Mapping the phase behavior for confined soft sphere fluids in contact with a bulk reservoir for a given bulk state point is complicated by a number of factors. The state of the pore fluid is influenced by the strength of the fluid–wall interaction, degree of confinement, and lattice symmetry of wall atoms in the case of pores with structured walls. Given the large degrees of freedom available for mapping out a complete phase diagram for nanoscopically confined soft sphere solids, it is possible that potentially stable frozen phases are yet to be identified. From the aforementioned similarities with confined colloids, clues to possible structures lie in the hard sphere phase diagram, which serve as a useful point of reference for the soft sphere system. The structures that have been identified in confined soft sphere solids that overlap with the hard sphere phase diagram are the $n\Delta$ and $n\Box$ phases. Other intermediate structures such as the ordered buckled phase between 1Δ and $2\Box$, the rhombic phase between $2\Box$ and 2Δ , as well as prism phases, observed in hard sphere systems,^{16,21} have not been reported for the confined soft sphere fluid. The random buckled phase, which is observed in experiments with colloidal suspensions,¹² characterized by increased out-of-plane movement while retaining in-plane triangular symmetry ($1\Delta_b$), has been observed in our earlier simulations of confined soft sphere systems.^{9,22}

In this manuscript, we investigate the structure of soft spheres confined between two mica surfaces. We use the interaction parameters that correspond to the octamethylcyclotetrasiloxane (OMCTS)–mica system. Although our focus in this system lies in the more general context of elucidating the behavior of frozen phases under confinement, the choice of the OMCTS–mica system is relevant to interpretation of results from surface force experiments. In a surface force apparatus, forces exerted by fluids confined between two mica surfaces are measured as a function of the separation between two surfaces.^{4,5} It is now well-established that oscillations in the solvation force as a function of surface separation are due to the formation and disruption of fluid layers parallel to the surface. Although forces

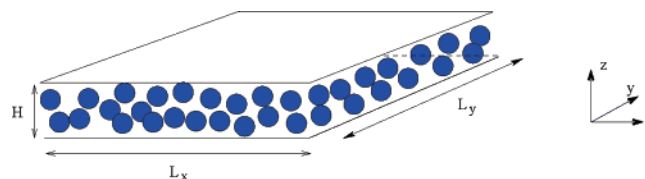


Figure 1. Schematic illustration of the pore of width H^* . Periodic boundary conditions are used in the x – y plane.

and the distances between mica surfaces can be measured extremely precisely in a surface force experiment, local ordering of the fluid molecules cannot be directly observed. The state of the fluid is inferred from the shear response of the confined fluid. An abrupt change in the shear viscosity of OMCTS is seen to occur when the confinement is changed from seven to six layers, suggestive of a confinement induced freezing transition occurring at a specific surface separation.^{32,33} An alternate interpretation to dynamic surface force experiments argues that confinement retards the dynamics of the fluid resulting in a more gradual glass-like transition.³⁴ Equilibrium Monte Carlo simulations in an isostress–isostrain ensemble indicate that freezing is not a necessary condition for inhomogeneous fluids confined between surfaces to exhibit a finite shear stress under the application of a strain. The study suggests that even disordered (perpendicular to confinement) films are expected to have rheological responses that are qualitatively similar to that of solids.^{35,36} More recently, direct observation of confined fluids at the nanoscale have been possible using X-ray scattering methods.³⁷ In these experiments, OMCTS is confined between single crystal silicon (root-mean-square roughness between 2 and 3 Å) and subjected to pressures ranging from 1.7 to 13.9 MPa. Structures with in-plane square symmetry provided the best match with the dispersion profiles when two and three fluid layers were accommodated between the surfaces. These findings are perhaps the first direct observation of structure under confinement in geometries and atomic dimensions for which extensive molecular simulations have been performed.

Previous simulation studies with the OMCTS–mica system have predominantly focused on the solvation force oscillations³⁸ and layering of the fluid as surface separation is changed. The effect of the relative alignments of the two mica surfaces on the structure of a single confined layer of OMCTS has also been investigated.^{39,40} In this manuscript, we carry out GCMC simulations for a wide range of surface separations which can accommodate one to eight fluid layers. Using appropriate bond order parameters and pair correlation functions, we map out the various phases that form for the OMCTS–mica system as well as evaluate the solvation force as the surface separation is changed. We illustrate that this system admits frozen phases that have not been observed in earlier confined soft sphere systems and discuss the relevance of our findings in the context of surface force experiments.

2. Theory and Simulation Procedure

2.1. Fluid–Wall Interactions: Smooth Mica Surface. Two models for the mica surface have been investigated in this study. Potassium atoms are excluded in the first model. The primary reason for treating the interactions in this manner was to enable comparison with a wide body of literature on freezing of soft sphere fluids between atomically smooth surfaces.³¹ In the second model, we explicitly include the potassium atoms.

A schematic of the simulation geometry is illustrated in Figure 1. The system is periodic in the x – y plane and of finite width,

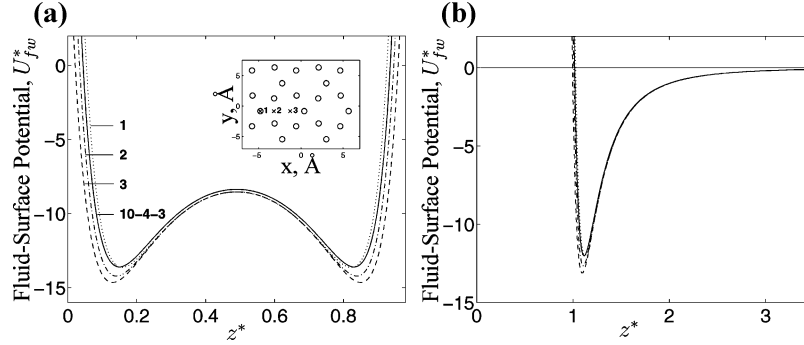


Figure 2. Comparison of the 10-4-3 OMCTS-mica interaction potential (eq 2) with the interaction of OMCTS with a structured mica surface constructed as described in the text. (a) $H^* = 2$. The interaction potentials are compared for different lateral positions of OMCTS with the oxygen atoms of the mica surface, as illustrated in the inset. (b) $H^* = 15$. The line types are similar to those of part a.

H , in the z direction. The interaction potentials for the mica system are similar to those used in earlier studies.^{38,40} The pairwise additive, fluid-fluid interactions are modeled using the 12-6 Lennard-Jones potential

$$u(r_{ij}) = 4\epsilon_{ff} \left[\left(\frac{\sigma_{ff}}{r_{ij}} \right)^{12} - \left(\frac{\sigma_{ff}}{r_{ij}} \right)^6 \right] \quad (1)$$

where ϵ_{ff} and σ_{ff} are the energy and molecular diameter, respectively, and r_{ij} is the distance between two particles. The mica surface is treated as being atomically smooth, and the fluid-wall potential is modeled using the 10-4-3 potential³⁸

$$U_{fw}(z) = 2\pi\rho_s\epsilon_{fw}\sigma_{fw}^2 \left[\sum_{k=0}^3 \left(\frac{2\sigma_{fw}^{10}}{5(z+k\Delta z_w)^{10}} - \frac{\sigma_{fw}^4}{(z+k\Delta z_w)^4} \right) - \frac{\sigma_{fw}^4}{3\Delta z_w(z+3\Delta z_w+\Delta z_{wl})^3} \right] \quad (2)$$

where z is the perpendicular distance between the fluid particle and the mica surface, $\rho_s = 0.12 \text{ \AA}^{-2}$ is the surface density of oxygen atoms, and $\Delta z_w = 2.2 \text{ \AA}$ is the spacing between consecutive layers of oxygen atoms. The last term in eq 2 represents the contribution from wall atoms beyond the fourth layer, where $\Delta z_{wl} = 2.5 \text{ \AA}$ is the average interlayer spacing of wall oxygen atoms. ϵ_{fw} is the fluid-wall interaction parameter, and σ_{fw} is the fluid-wall interaction diameter.

We compared the OMCTS-mica interaction using eq 2 with that predicted with a structured wall representation of the mica surface corresponding to 2M Muscovite mica.⁴¹ We model the structured mica surface as a single layer of oxygen atoms with the background potential given by eq 2, with the summation index starting at $k = 1$. The separation between two opposing surfaces is measured from the first layer of oxygen centers. The dimensions of the structured mica surface are $L_x = 94.428 \text{ \AA}$ and $L_y = 91.79 \text{ \AA}$, and a potential cut-off of $4\sigma_{ff}$ was used while evaluating the interaction potential. The OMCTS-mica interaction parameters are computed using Lorentz-Berthelot mixture rules.

$$\sigma_{fw} = \frac{\sigma_{ff} + \sigma_{ww}}{2} \quad \text{and} \quad \epsilon_{fw} = \sqrt{\epsilon_{ff}\epsilon_{ww}} \quad (3)$$

The comparison shown in Figure 2 indicates that the smooth wall approximation (eq 2) provides an excellent representation of the fluid-wall interaction for the OMCTS-mica system. The potential showed little variability when OMCTS was moved in different lateral (x - y) positions over the oxygen atoms of the

TABLE 1: Reduced Quantities Used in This Work^a

quantity	reduced unit
solvation pressure	$f_z^* = f_z\sigma_{ff}^3/\epsilon_{ff}$
surface separation	$H^* = H/\sigma_{ff}$
pressure	$P^* = P\sigma_{ff}^3/\epsilon_{ff}$
temperature	$T^* = kT/\epsilon_{ff}$
density	$\rho^* = \rho\sigma_{ff}^3$
activity	$Z^* = Z\sigma_{ff}^3$

^a ϵ_{ff} and σ_{ff} are the Lennard-Jones parameters for the fluid-fluid interaction.

TABLE 2: Bulk Fluid State Points^a

state point	ρ^*	T^*	Z^*
A	0.757	0.883	0.0103
B	0.89	0.8443	0.112

^a Points A and B are illustrated in the bulk Lennard-Jones phase diagram shown in Figure 3.

structured mica surface, as illustrated in the inset of Figure 2a. Since we are concerned with the structure of frozen phases, at smaller surface separations, we also carried out a few simulations with the structured wall model for comparison with the smooth wall potential.

2.2. Fluid-Wall Interactions: With Potassium Atoms (Mica-K). In the second model for the mica surface, potassium atoms are explicitly included.^{42,43} We refer to this system as the mica-K system to distinguish it from the situation when potassium atoms are absent. The mica surface was modeled using the 10-4-3 smooth wall potential given by eq 2 with potassium atoms rigidly placed at a distance of 1.53 \AA from the surface. Each unit cell of muscovite mica has two potassium ions in a unit cell. In order to mimic the surface resulting from cleaving mica, we randomly removed one potassium ion from each unit cell after preparing the periodic surface of dimension $L_x = 94.428 \text{ \AA}$ and $L_y = 91.79 \text{ \AA}$. The second mica surface was constructed in a similar fashion. The resulting potassium ion surface density^{44,45} is $2.1 \times 10^{14} \text{ atoms/cm}^2$. In comparison, the oxygen surface density is $12.5 \times 10^{14} \text{ atoms/cm}^2$. We carried out GCMC simulations for selected surface separations in the range $1.2 \leq H^* \leq 8.1$. The LJ potential parameters⁴⁶ for potassium are $\epsilon_{kk} = 50.32 \text{ K}$ and $\sigma_{kk} = 3.331 \text{ \AA}$.

2.3. Bulk Fluid Conditions. We have investigated two state points for the bulk conditions of OMCTS given in Table 2. The first state point³⁸ (A) corresponds to a reduced temperature, $T^* = kT/\epsilon_{ff} = 0.883$, and a reduced density, $\rho^* = \rho\sigma_{ff}^3 = 0.757$. The location of the state point (A) on the bulk LJ phase diagram is illustrated in Figure 3. It lies in the proximity of the liquid-vapor coexistence curve and corresponds to a pressure of 1 atm. Unless otherwise stated, all simulations correspond to the bulk

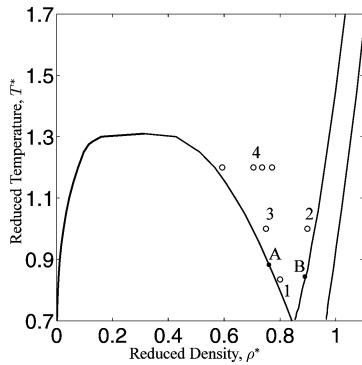


Figure 3. Bulk Lennard-Jones phase diagram in the T^* – ρ^* plane illustrating the location of the bulk state points (see Table 2) for OMCTS used in this study. State point A used in this study is similar to bulk conditions used in previous studies of OMCTS confined in mica.^{38,51} State point B is located in the proximity of the freezing line. The liquid–vapor coexistence data are from Lofti et al.,⁵² and the liquid–solid coexistence data, from Agarwal and Kofke.⁴⁷ State points 1,³ 2,⁹ 3,⁶ and 4⁵³ were used in earlier confined fluid studies where the solvation force and fluid structure were evaluated.

TABLE 3: Fluid–Fluid and Fluid–Wall Potential Parameters Used in This Study for State Points A and B Shown in Figure 3

parameter	OMCTS (A)	OMCTS (B)	oxygen
ϵ_{ff} (K)	343.095	351.36	117.958
σ_{ff} (Å)	7.7	7.7	
σ_{ww} (Å)			2.71

conditions of state point A. We also carried out simulations corresponding to state point B in the phase diagram. This state point lies in the proximity of the freezing line and has been parametrized to yield conditions in surface force experiments³² carried out at 296.65 K which is 6.5° above the bulk freezing point of OMCTS (290.15 K). The interaction energy, ϵ_{ff} , was reparametrized to the bulk freezing point of OMCTS using the freezing line data for LJ fluids from Agarwal and Kofke.⁴⁷ The reduced density was also chosen to match the density of OMCTS reported at 293 K which is 0.9561 gm/cc. Hence, state point B which corresponds to $T^* = 0.8443$ and $\rho^* = 0.89$ has an elevation of 6.5 K from the freezing temperature of OMCTS.³² The pressure, however, of the bulk liquid is significantly higher. The interaction parameters used in our GCMC simulations for both state points A and B are given in Table 3. Bulk fluid GCMC simulations with a reduced box size of $8\sigma_{\text{ff}}$ and a $4\sigma_{\text{ff}}$ potential cutoff were carried out for both state points to check the accuracy of the activities obtained from the equation of state.⁴⁸ In the case of state point B, a few GCMC simulations (with long range corrections) at different activities were run in order to obtain the activity corresponding to the target bulk density.

2.4. Layer Density Distributions. The formation and disruption of layers was mentioned using the layer density distribution evaluated using

$$\rho(z) = \frac{\left\langle N\left(z - \frac{\Delta z}{2}, z + \frac{\Delta z}{2}\right) \right\rangle}{A\Delta z} \quad (4)$$

where $\langle N(z - \Delta z/2, z + \Delta z/2) \rangle$ is the ensemble averaged number of atoms in a bin of thickness Δz in the z direction and A is the area of the fluid layer in the x – y plane. A bin width of $\Delta z = 0.025\sigma$ was used to evaluate the density.

2.5. Solvation Pressure. The solvation pressure for the fluid confined in a slit pore of area A is defined as^{1–3,6}

$$f_z = \frac{1}{2A} \sum_{i=1}^N \left(\frac{dU_{\text{fw}}(z_i + H/2)}{dz_i} - \frac{dU_{\text{fw}}(H/2 - z_i)}{dz_i} \right) \quad (5)$$

where U_{fw} is the fluid–wall interaction potential (eq 2) and z_i is the distance of the fluid particle from the center of the simulation box. The disjoining pressure is defined as the difference between the solvation pressure and the bulk pressure of the fluid in equilibrium with the pore. In the case of the structured mica surface, the solvation pressure contribution from the first layer of discrete oxygen atoms is added to the background smooth wall potential which excludes the first-layer contribution in eq 2.

2.6. Bond Angle Order Parameters. In-plane order within a fluid layer is evaluated using the in-plane bond angle order parameter. The bond angle order parameter is computed using^{17,18}

$$\psi_n = \left\langle \frac{1}{N_b} \left| \sum_{j=1}^{N_b} \exp(in\theta_j) \right| \right\rangle, \quad n = 4, 6 \quad (6)$$

where θ_j is the bond angle formed between an atom and its nearest neighbors with reference to a fixed reference frame. While computing the bond angles defined above, a cutoff of $1.25\sigma_{\text{ff}}$ was used to determine the nearest neighbor bond distances. The bond order parameters are computed for individual layers as well as averaged over the different layers in the pore to yield a pore averaged value. We point out that the bond order parameters defined above can be used only to differentiate between lattices with square and triangular symmetry within an individual fluid layer.

2.7. In-Plane Pair Correlation Function. The in-plane pair correlation function is computed within individual layers of thickness Δz_1 in the pore using

$$g_1(r) = \left\langle \frac{1}{N_1} \sum_{i=1}^{N_1} \frac{n_i(r + \Delta r/2, r - \Delta r/2; \Delta z_1)}{\rho_1(z) 2\pi r \Delta r} \right\rangle \quad (7)$$

where $n_i(r + \Delta r/2, r - \Delta r/2; \Delta z_1)$ is the number of particles from particle i at a distance r , located in a cylindrical shell of thickness Δr and height Δz_1 containing N_1 particles. $\rho_1(z)$ is the areal density of the layer of thickness Δz_1 . Boundaries of each layer are obtained from the corresponding layer density distributions defined in eq 4.

2.8. Simulation Details. All results are reported in reduced units, as shown in Table 1. For the 10–4–3 potential a square simulation box was employed in all cases with periodic boundary conditions in the x – y plane, as illustrated in Figure 1. In order to assess the influence of finite size effects, GCMC simulations were carried out for simulation box lengths $L_x = L_y = 9, 12$, and $15\sigma_{\text{ff}}$. In all cases, we compared the order parameters, solvation force, and ensemble averaged number density. The results, as inferred from the sequence of frozen structures, between the 12 and $15\sigma_{\text{ff}}$ box sizes showed little variation. Hence, all results reported in this manuscript correspond to the $12\sigma_{\text{ff}}$ simulation box. In the case of the atomically smooth mica surfaces, GCMC (μVT) simulations for smaller pores consisted of $(400\text{--}600) \times 10^6$ Monte Carlo moves out of which the last $(200\text{--}300) \times 10^6$ moves were used for evaluating properties. In some cases, we carried out a few simulations at the same pore separation with a different random number seed. The greatest deviation in the number of particles (<5%) was found at pore separations where a transition from one to two and two to three layers occurred. This variation did not affect the symmetry of the observed phase.

For larger ($H^* > 4.8$) pores, 900×10^6 MC moves were used, out of which the last 200×10^6 moves were used for property evaluation. In the case of the structured mica surface as well as with the mica-K surfaces, simulation run lengths consisted of 200×10^6 MC moves out of which 100×10^6 moves were used for computing averages. Each Monte Carlo move consists of an attempted addition, deletion, and displacement with equal probability.⁴⁹ All GCMC simulations were started with an empty simulation box.

In addition to the Monte Carlo simulations, we also carried out a series of microcanonical (NVE) molecular dynamics simulations to assess the stability of the various frozen phases at selected surface separations. These also served as a check on the accuracy of our simulations. The molecular dynamics simulations were carried out with the ensemble averaged number of particles obtained from the GCMC simulations for surface separations ranging from $H^* = 1.3$ to $H^* = 6.0$ for which pair correlation function data are presented in this manuscript. In all cases, the structural properties, such as the density distribution, solvation force, order parameters, and in-plane pair correlation functions, were in excellent agreement with those obtained from GCMC simulations. A few molecular dynamics simulations were also carried out at different temperatures ranging from 275 to 340 K for surface separations corresponding to $H^* = 1.45, 1.65, 1.7, 1.84$, and 1.96 . The symmetry of the structures observed at these separations was unaltered, and the structures were found to be stable in this temperature range.

3. Results

In this section, we discuss the results for the atomically smooth mica system.

3.1. Order Parameters and Lattice Transitions. The bond order parameters, Ψ_4 and Ψ_6 , are plotted as a function of surface separation, H^* , in Figure 4a. Ψ_4 and Ψ_6 as defined in eq 6 distinguish phases that form with either in-plane triangular or square symmetry and provide the first indication of solid–solid transitions. In the single-layer regime ($n = 1$), only structures with triangular symmetry are observed. The bond order parameters reveal that $n\square$ -to- $n\Delta$ lattice transformations are observed up to $n = 3$ (three layers). At larger surface separations where four to six layers are accommodated, only lattices with triangular symmetry are observed. In this regime, the addition of a new layer is accompanied by a sharp increase in the values of Ψ_6 (≥ 0.75). Upon the addition of a new layer, the maximum value of Ψ_6 decreases in the range $n = 4$ –7. At larger surface separations when $n = 7$ ($H^* > 6.85$), the sharp rise in the order parameter, accompanying the addition of a new fluid layer, is absent and the low value of Ψ_6 reveals increased in-plane disorder in the confined fluid. Examination of the layer density distributions reveals that the formation of distinct layers within the pore is also disrupted beyond the six-layer regime.

It is instructive to examine the contribution to the order parameter from the contact layer and inner fluid layers separately. This is illustrated in Figure 4b where the order parameter for the contact and inner layers are shown for $n \geq 3$. The order parameter for the fluid adjacent to the mica surface reveals a frozen contact layer even when ordering in the adjacent inner layers is disrupted. Simulations carried out at larger surface separations reveal that the frozen contact layer is present even up to $H^* = 20$ where densities in the pore interior are similar to the bulk density of the fluid in equilibrium with the pore. Since the contact layer is completely frozen for both $n = 6$ and $n = 7$, an indication of the extent of freezing in this range of surface separations ($5.8 < H^* < 6.8$) can be better perceived

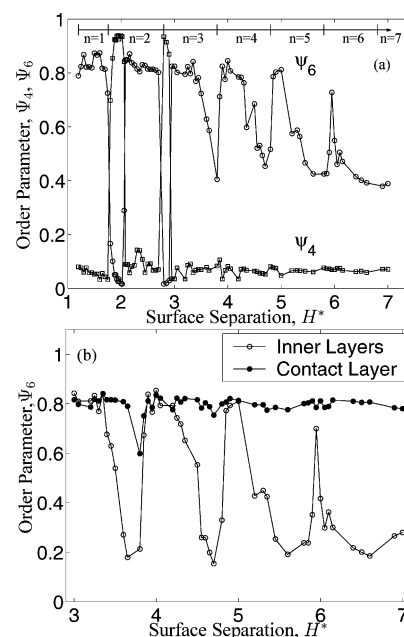


Figure 4. (a) In-plane order parameters Ψ_4 and Ψ_6 as a function of the reduced surface separation, H^* . The order parameters illustrate the presence of square lattices for $n = 2$ and 3 . For $n \geq 4$, only lattices with triangular symmetry are observed. (b) The large value of Ψ_6 for the fluid adjacent to the mica surface (filled circles) reveals the presence of a frozen contact layer even when the inner layers are fluidlike. This situation persists for surface separations as large as $H^* = 20$ (not shown). The order parameters computed without including the contribution from the contact layers indicates that the inner layers are frozen in a narrow region around $H^* = 6.0$ where $n = 6$. Beyond this, only liquidlike inner layers are observed.

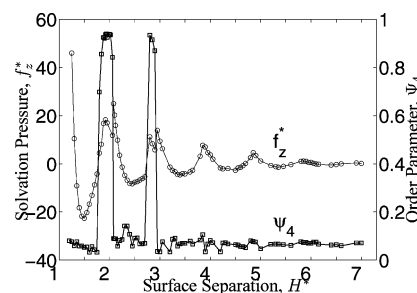


Figure 5. Solvation force and Ψ_6 as a function of surface separation, H^* . The transition from square to triangular lattices at $n = 2$ and 3 occurs with a split in the solvation force peaks. Beyond $n = 3$, lattices with square symmetry are absent and only lattices with triangular symmetry are formed.

from examining the variation of the average layer order parameter excluding the contact layer. The value of Ψ_6 for the inner layers varies from 0.74 at $H^* = 6.0$ ($n = 6$) to 0.3 at $H^* = 7.0$ ($n = 7$). Note that the larger value of $\Psi_6 = 0.4$ at $H^* = 7.0$ shown in Figure 4a is due to the contribution from the high in-plane order in the layers adjacent to the mica surface. The order parameter averaged only over the inner layers indicates a rapid increase in disorder beyond $H^* = 6.0$, indicating that the ordered six-layered system exists in a narrow range around $H^* = 6.0$.

Figure 5 illustrates the variation of the solvation pressure as a function of surface separation. In addition to the broad oscillations due to the formation and disruption of layers, the second and third peaks are split. The order parameter (Ψ_4) superimposed on the solvation pressure data indicates that the split peaks occur in the transition from $n\square$ to $(n)\Delta$ lattices. The split peaks, which are a distinct signature of the transition

TABLE 4: Summary of the Observed Lattice Structures and the Range over Which Various Phases Are Observed^a

structure	H^*	structure	H^*
1Δ	$1.20 \leq H^* < 1.55$	4Δ	$3.85 \leq H^* < 4.55$
$1\Delta_b$	$1.55 \leq H^* < 1.72$	$4CL\Delta$	$4.55 \leq H^* < 4.85$
$2B$	$1.76 \leq H^* < 1.88$	5Δ	$4.85 \leq H^* < 5.20$
$2\Box$	$1.88 \leq H^* < 2.08$	$5CL\Delta$	$5.20 \leq H^* < 5.85$
2Δ	$2.08 \leq H^* < 2.45$	$6CL\Delta$	$5.85 \leq H^* < 5.92$
$2\Delta_b$	$2.45 \leq H^* < 2.80$	6Δ	$5.92 \leq H^* < 6.00$
$3\Box$	$2.80 \leq H^* < 2.92$	$6CL\Delta$	$6.00 \leq H^* < 6.85$
3Δ	$2.92 \leq H^* < 3.55$	$7CL\Delta$	$6.85 \leq H^* < 7.85$
$3CL\Delta$	$3.55 \leq H^* < 3.85$		

^a n , number of layers; B, line buckled; CL, contact layer frozen.

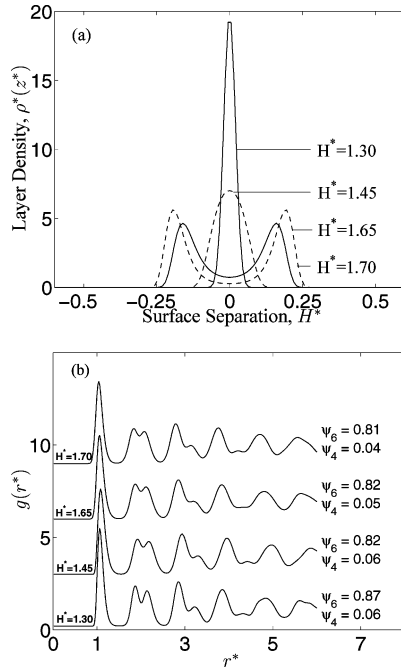


Figure 6. (a) Density distributions and (b) in-plane pair correlation functions in the single-layer regime ($n = 1$). The in-plane pair correlation functions illustrate the presence of a triangular lattice even when there is significant out-of-plane movement at the larger surface separations, $H^* = 1.65$ and 1.7 . This buckled phase is denoted as the $1\Delta_b$ phase.

between lattice symmetries^{8,9,22,27} for a fixed number of fluid layers, are not found beyond the three-layer regime ($H^* \geq 3.8$) where frozen phases with triangular symmetry are observed.

3.2. Buckled Phases: One and Two Layers. In order to ascertain the presence of intermediate phases between the triangular and square lattices, we resort to a detailed examination of the particle snapshots and in-plane pair correlation functions. Table 4 summarizes the various structures and the range of surface separations where the structures were observed. Figure 6a illustrates the density distributions in the single-layered regime. Pair correlation functions (Figure 6b) indicate that the pore fluid is frozen into a lattice with triangular symmetry. The order parameter (Ψ_6) indicates that the triangular symmetry is retained up to $H^* = 1.73$. Beyond a surface separation of about $H^* = 1.55$, the particles are no longer restricted to the $z = 0$ plane but undergo significant out-of-plane motion or buckling. Figure 7b illustrates the in-plane triangular symmetry of this phase at $H^* = 1.65$, and buckling is clearly visible in the side view particle snapshot shown in Figure 7a. Dark circles in the top view snapshot which distinguish particles with positive and negative z coordinates illustrate that buckling is random. We have referred to this phase as the $1\Delta_b$ phase where buckling,

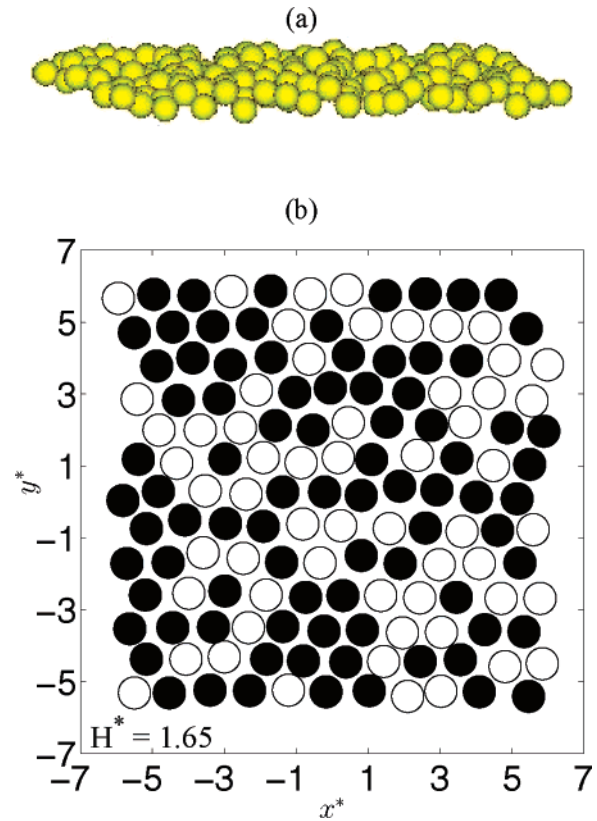


Figure 7. Snapshots of a lateral (top) and top view (bottom) of the $1\Delta_b$ phase at $H^* = 1.65$ where random buckling is observed. The dark circles correspond to the atoms with positive z coordinates.

albeit random, helps retain in-plane triangular symmetry of the confined fluid. This phase has also been observed in solid–solid transformation of methane confined in graphite⁹ as well as in experiments of colloidal suspensions confined between glass plates.¹²

As the surface separation is increased beyond $H^* = 1.76$, the $1\Delta_b$ phase transforms to the $2B$ phase which lies between the 1Δ and $2\Box$ systems. Figure 8a illustrates both the top and side views of a snapshot at $H^* = 1.84$ where the buckled phase, $2B$, is observed. The $2B$ phase is characterized by alternate rows of particles displaced with respect to each other in the z direction. The pore fluid is arranged into two distinct layers, as illustrated in Figure 9a at this surface separation. The pair distribution function as well as the order parameters (Figure 9b) reveal that the lattice symmetry is no longer triangular. The large value of Ψ_4 indicates that the relative orientation between first neighbor bonds (within a layer) of a given atom is a multiple of 90° . This form of buckling, observed in the $2B$ phase, also referred to as linear buckling, has been reported previously for confined hard spheres,^{17,21} as well as observed in simulations of soft colloids.¹⁹ To our knowledge, this phase has not been documented for confined soft spheres. In order to study the influence of system size on the $2B$ structure, we carried out simulations with a periodic box of side $20\sigma_{ff}$. Figure 8b illustrates the side and top view snapshots, respectively, for the large system. The buckled phase is clearly observed; however, at the larger system sizes (Figure 8b), subdomains with different orientations of buckling are observed. As the surface separation is increased, the transition from $2B$ to $2\Box$ occurs. A typical pair correlation function of the $2\Box$ phase is illustrated in Figure 9b at $H^* = 1.96$. A top view snapshot of the square phase is illustrated in Figure 10.

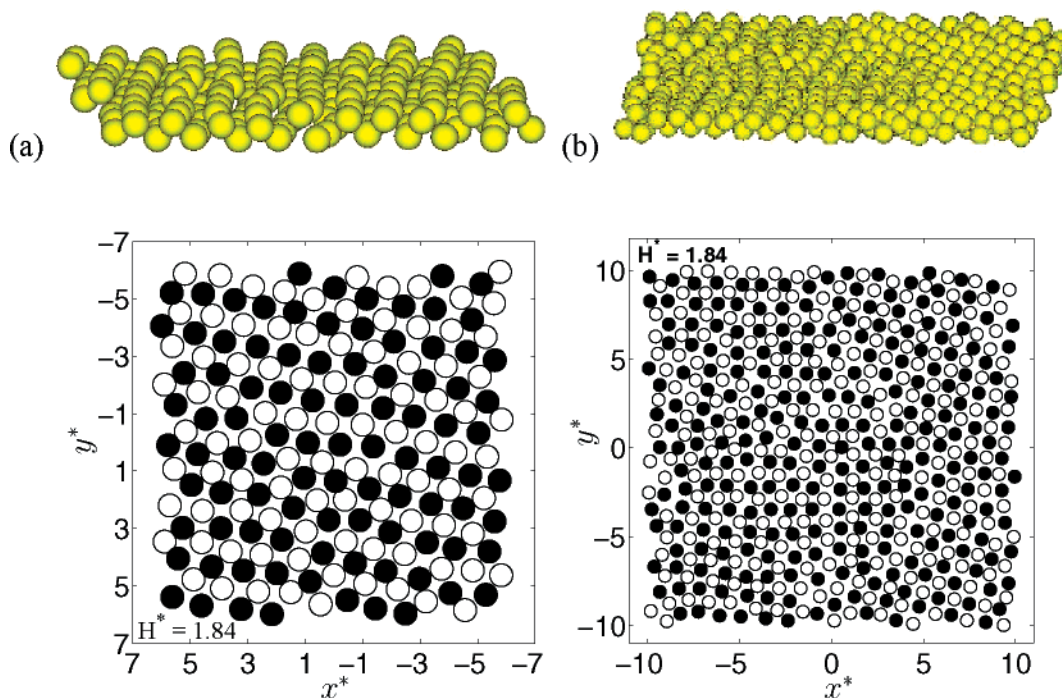


Figure 8. Snapshots of a lateral and x – y view of the line buckled 2B phase at $H^* = 1.84$. Part a corresponds to a periodic box of side $12\sigma_{\text{ff}}$, and part b corresponds to a periodic box of side $20\sigma_{\text{ff}}$. The line buckled phase is observed at both system sizes. At the larger system size (b), coexisting domains and corresponding grain boundaries are also observed.

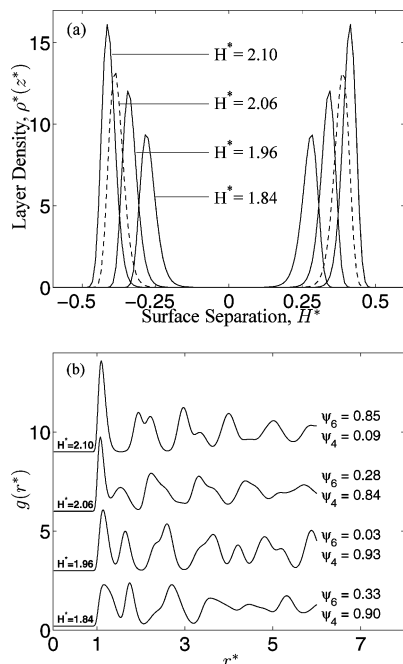


Figure 9. (a) Density distributions in the $n = 2$ regime with corresponding in-plane pair correlation functions (b), illustrating the transition from the line buckled 2B ($H^* = 1.84$) to $2\Box$ and 2Δ as surface separation is increased.

For $H^* \geq 2.08$, the 2Δ phase is observed. Lattices with in-plane triangular symmetry are found up to a surface separation of $H^* = 2.45$ above which a new layer is added. For $2.08 \leq H^* < 2.8$, the atoms in each layer occupy the threefold hollow sites of the lattice formed by the adjacent layer. At larger surface separations, the atoms move out of the threefold sites with increased out-of-plane movement. In this regime, there is little correlation (as observed from the particle snapshots) between atoms in adjacent layers. This phase is referred to as the $2\Delta_b$ phase and occurs for $2.45 \leq H^* < 2.8$. A similar situation was

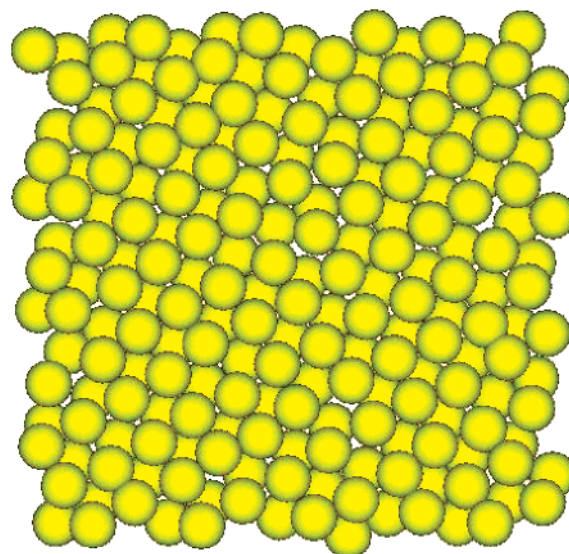


Figure 10. Particle x – y snapshot of the $2\Box$ phase which occurs at $H^* = 1.96$.

observed in earlier studies where solid–solid transitions have been observed.^{9,10}

3.3. Phases at Larger H^* : Three to Seven Layers. As the surface separation is increased beyond the bilayer regime ($H^* = 2.8$), the last square-to-triangular lattice transition is observed within the range $2.8 \leq H^* < 2.92$, where $n = 3$. The range of pore widths over which $3\Box$ is stable (Table 4) is narrower than the range for the $2\Box$ phase. Beyond $H^* = 3.85$ where four fluid layers form ($n \geq 4$), only phases with in-plane triangular symmetry are observed when the pore fluid is frozen. In addition to fully frozen phases, we also observe regimes where only the contact layer is frozen and inner layers are liquid-like. This situation occurs prior to the addition of a new fluid layer. These phases are denoted as $n\text{CL}\Delta$ in Table 4 and occur for $n \geq 3$. For $H^* > 6.0$ where the pore fluid is no longer frozen, the pore

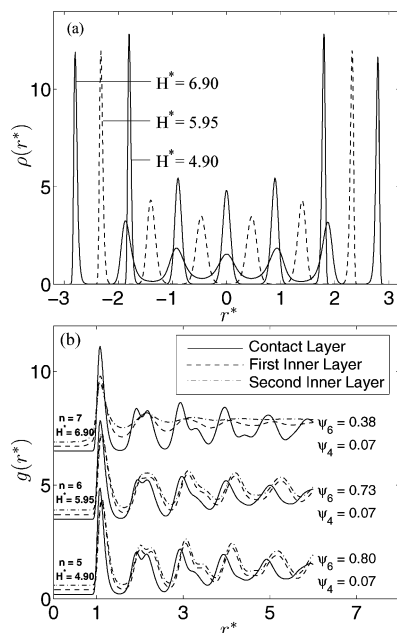


Figure 11. (a) Density distributions and (b) in-plane pair correlation functions for the contact layer and first and second inner layers are illustrated for $n = 5, 6$, and 7 . The pair correlation functions at a given number of layers are y -offset by 0.2 units for clarity. The order parameters represent averages over all of the layers within the pore. The pair correlation functions reveal frozen phases at $n = 5$ and 6 , and at $n = 7$, the pore consists of a frozen contact layer and liquid-like inner layers.

is characterized by a frozen contact layer with triangular symmetry coexisting with disordered liquid-like inner layers.

Figure 11 illustrates the density distributions and pair correlation functions for $n = 5, 6$, and 7 . We picked the surface separations at which layers are well-defined with high in-plane order. These correspond to $H^* = 4.9, 5.95$, and 6.9 for $n = 5, 6$, and 7 , respectively. Figure 12 has the corresponding snapshots of particle configurations. The density distributions (Figure 11a) and snapshots reveal the presence of well-defined layers for $n = 5$ and 6 . At $n = 7$, layering within the pore is disrupted, although a well-defined layer adjacent to the mica surface is visible. Over this range of surface separations, the Ψ_6 order parameter computed for the contact layer alone indicates a high degree of in-plane order, as illustrated in Figure 4b. The corresponding pair correlation functions are illustrated in Figure 11b where the contact layer possesses a high degree of in-plane order for all three surface separations. At $H^* = 6.9$, the inner layers lose in-plane order, becoming more liquid-like. Some residual order is retained in the second layer at $H^* = 6.9$ due to templating with the ordered contact layer. At $H^* = 5.95$ and 6.9 , both the first and second inner layers reveal ordered in-plane structures. We note that the relative order, both in plane and out of plane (layering), is significantly greater at $n = 6$ ($H^* = 5.95$) when compared with the $n = 7$ ($H^* = 6.9$) pore. The inner layers at $n = 6$ ($H^* = 5.95$) are much more loosely packed and defective. This looser packing of the inner layers is revealed in the pair correlation functions shown in Figure 11b where the peaks are broader and more spread out.

For pores where $n \geq 3$, the stacking sequence of different layers which reflect the relative positions of atoms in one layer with respect to an adjacent layer is an added degree of freedom. For $n = 3-5$, the predominant stacking sequence was ABA, and on occasion, the ABC stacking sequence was also observed. For $n = 4$, mixed ABAB and ABCA stacking was also observed at $H^* = 4.2$ and 4.3 . Since stacking was inferred only from

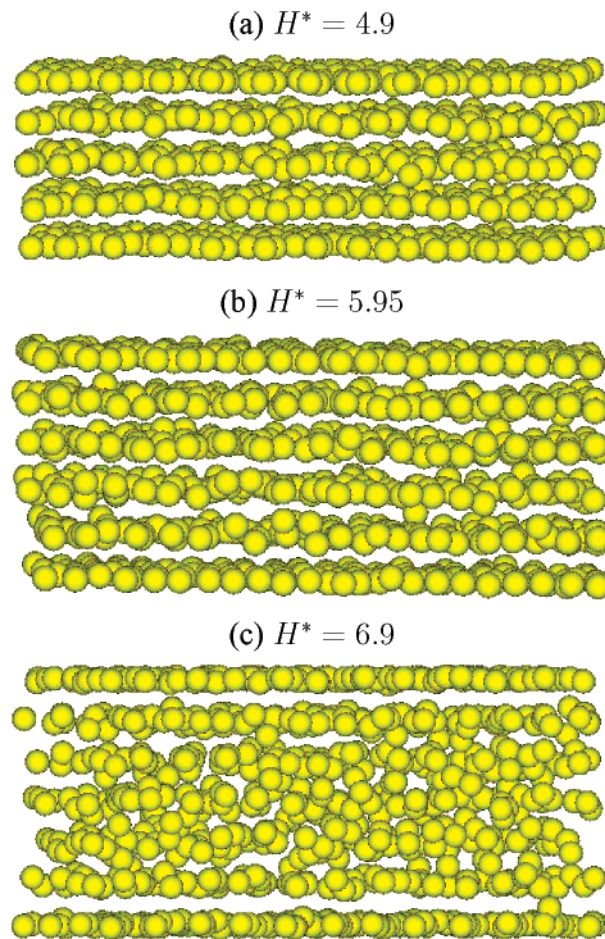


Figure 12. Snapshots for the $n = 5, 6$, and 7 layers whose corresponding pair correlation functions and density distributions are shown in Figure 11. The presence of a frozen contact (outermost) layer at all surface separations is clearly observed. Increased disorder within the inner layers is seen at $n = 7$.

snapshots at the end of the simulation, these sequences are only representative and cannot be used to draw conclusions about an ensemble averaged situation. In the narrow range of surface separations where freezing was observed for $n = 6$, only ABABAB stacking sequences were observed. We note that in previous simulations a change in stacking from ABA to ABC was observed for $n = 3$,^{9,10} and predominantly, ABAB sequences were encountered for $n > 3$.²⁴

3.4. Number Density. The ensemble averaged number, $\langle N \rangle$, of particles as a function of surface separation is illustrated in Figure 13. Table 4 summarizes the various structures and range of surface separations where different confined fluid structures were observed. Steps in $\langle N \rangle$ as a function of H^* are indicative of layering transitions. The sharpness of the steplike features that are observed when a new layer is admitted is indicative of a layering transition. In this study, the layering transition is also associated with a freezing transition up to $n = 6$. In the $1\Delta \rightarrow 1\Delta_b \rightarrow 2B$ regime, the step in the number is more gradual due to the presence of the intermediate buckled phases. Distinct steps in $\langle N \rangle$ were not observed during the transition from square to triangular symmetry. The results from our earlier study⁹ suggest that the presence of secondary steps, between lattice symmetries, for a given set of fluid and pore interaction parameters could be related to the activity of the bulk fluid that is in equilibrium with the pore. In our earlier study with the methane-graphite⁹ system, where the reduced bulk fluid activity was an order of magnitude larger than the present study, we found distinct steps

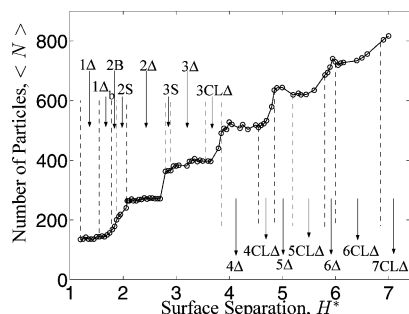


Figure 13. Ensemble average number density $\langle N \rangle$ vs surface separation, H^* . The transition from $n = 1$ to $n = 2$ is gradual due to the presence of the intermediate buckled phases, $1\Delta_b$ and $2B$. The steps associated with the inclusion of a new layer are sharp at the smaller surface separations, becoming progressively more gradual with an increase in surface separation, H^* . The transition in $\langle N \rangle$ from $n = 6$ to $n = 7$ is the most gradual among all of the transitions examined. The surface separations at which the different phases are observed are summarized in Table 4.

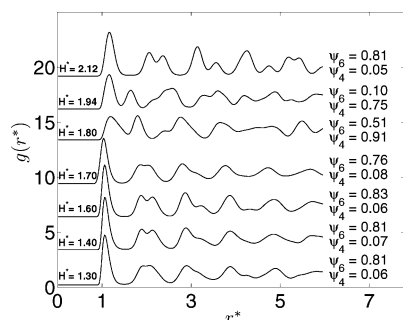
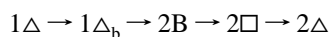


Figure 14. Pair correlation functions for the structured mica surface in the $n = 1$ and $n = 2$ layered regimes. The sequence of transitions is very similar to that obtained with the smooth walled mica surface, indicating that the presence of discrete oxygen atoms plays a minor role in influencing the pore structure for the OMCTS–mica system.

in $\langle N \rangle$ in all of the transformations between square and triangular symmetry. At higher surface separations, the steplike changes in $\langle N \rangle$ decrease, and beyond $n = 6$, the steps get gradually weaker. This is consistent with our findings based on the order parameters (Figure 4) and pair correlation functions that the fluid gets rapidly disordered beyond the onset of the six-layered regime.

3.5. Structured Mica Surface. In order to assess the influence of the wall structure on the freezing behavior, we carried out simulations with a structured mica surface at selected surface separations in the one- and two-layered regimes, where the effect of the mica structure is expected to have the greatest influence on the state of the fluid. The pair correlation functions are illustrated in Figure 14 for surface separations ranging from $1.3 \leq H^* \leq 2.12$. The results indicate that the following sequence of transitions



which was observed with the smooth wall potential for the mica surface are preserved with the structured walls as well. We did not carry out any simulations beyond the three-layered regime, as differences, if any, are more likely to manifest themselves at the smaller surface separations. The potential energy differences between the structured and smooth wall models at the smaller surface separations (albeit small) are the greatest with the differences diminishing as the surface separation is increased (Figure 2).

3.6. Influence of Potassium on Freezing: Mica–K. In the mica–K system, we carried out GCMC simulations at selected

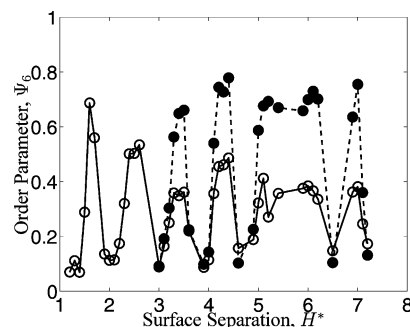


Figure 15. Ψ_6 order parameters for inner (filled circles) and contact layers (open circles) for the mica–K system equilibrated with state point B. In the single-layer regime, only the randomly buckled phase is observed. Freezing of the inner layers is observed for surface separations that can accommodate three to seven layers. The moderate value of the order parameter for the contact layer suggests the presence of some residual order. The values of the layer averaged, Ψ_6 order parameter for the mica–K system with state point A (not shown) lie below 0.25 for pore widths greater than $H^* = 2.0$.

surface separations for both bulk state points A and B (Figure 3). In the case of bulk state point A, the inclusion of potassium ions on the surface disrupted the extended freezing behavior and solid–solid transformations. Interestingly, the only frozen phase observed was the randomly buckled phases at $H^* = 1.6$ and $H^* = 1.7$ where $\Psi_6 = 0.7$ and 0.62 , respectively. As H^* is increased, the fluid is able to form layers; however, the presence of potassium results in a spreading of the density distribution in the contact layer adjacent to the mica surface. This is sufficient to disrupt in-plane order, thereby preventing the formation of frozen phases.

In the case of state point B, which lies close to the liquid–solid coexistence line, we observed a rather unexpected phenomenon. At smaller pore widths similar to state point A, we observed the randomly buckled triangular phase at $H^* = 1.6$ and 1.7 . As H^* is further increased, the outer layers remain fluidlike due to the presence of potassium. However, the inner layers begin to progressively get more solid-like with increasing pore width. The Ψ_6 order parameters for the mica–K system are illustrated in Figure 15 where the inner and contact layer order parameters are compared separately for state point B. The first signature of freezing in the inner layers was observed at $H^* = 3.4$, $n = 3$. This situation where the contact layers are liquid-like with freezing occurring in the inner layers is observed up to $n = 7$. From the order parameters illustrated in Figure 15, inner layer freezing was the strongest for $n = 4, 5$, and 6 , getting weaker for $n = 7$. At $n = 7$, inner layer freezing was observed for $H^* = 6.9$ and 7.0 with liquid-like inner layers for $H^* > 7.1$. Inner layer freezing was not observed at $H^* = 7.9$ or 8.0 ($n = 8$).

We compared the density distributions at selected pore widths in Figure 16. Here, the density distributions for the mica–K system for both state points A and B are compared with the density distribution in the absence of potassium equilibrated with state point A discussed earlier in the manuscript. In all cases, the extent of layering and the location of the contact layer are similar. When potassium is present, a small shoulder in the contact layer is observed and the height of the density peak is reduced. This is sufficient to disrupt the formation of the frozen contact layer in the case of both state points A and B (Figure 15). When the state point is shifted from A to B for the mica–K system, the density in the inner layers and the intensity of layering is seen to increase. This results in freezing of the inner layers with triangular symmetry, as seen in the order parameters given in Figure 15. The pair correlation functions for the

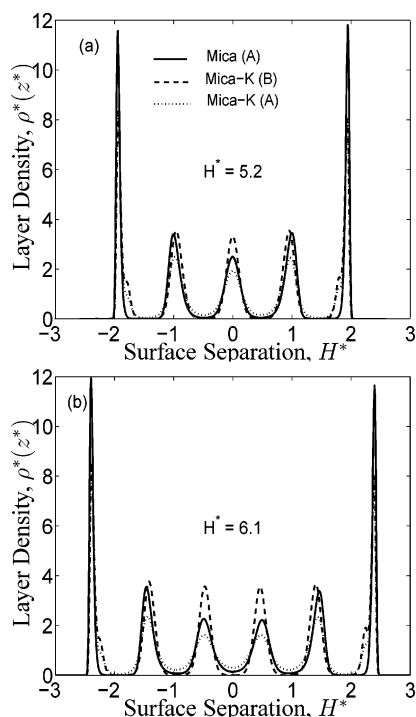


Figure 16. Density distribution comparing the degree of layering for the atomically smooth mica system equilibrated with state point A, with the mica-K system equilibrated with state points A and B. Layering is not disrupted in the mica-K system; however, the intensity of the inner peaks and the degree of layering increases when the state point is changed from A to B. This leads to the presence of frozen inner layers with state point B. Corresponding pair correlation functions are shown in Figure 17.

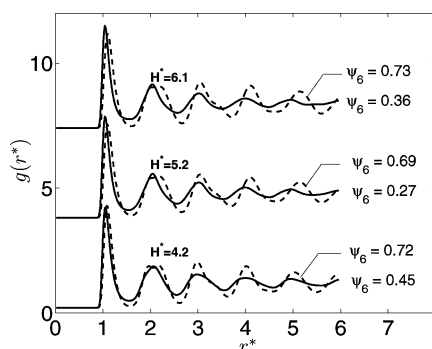


Figure 17. Pair correlation functions indicate increased order in the inner layers when compared with the contact layer for the mica-K system. Results from GCMC simulations for the mica-K system carried out with bulk state point B which lies close to the bulk fluid freezing line.

mica-K system for state point B are shown in Figure 17 at selected pore widths. The contact layer and inner layer (averaged) pair correlation functions are contrasted. These illustrate that the inner layers are frozen into lattices with in-plane triangular symmetry while the contact layers are disordered. The moderate values of the in-plane order parameters of the contact layer indicate that some residual ordering is still present.

4. Discussion

4.1. Atomically Smooth Mica Surface. Molecular simulations have established that confined soft spheres can freeze and undergo solid–solid transitions between lattices of square and triangular symmetry. Unlike hard sphere fluids confined between hard walls, the increased number of parameters in the soft sphere

system complicates a complete mapping of the phase diagram. For a given set of Lennard-Jones fluid–fluid and fluid–wall interaction parameters, the location of the bulk state point which is in equilibrium with the pore is seen to play an important role in determining the phase of the pore fluid.^{24,25} Table 4 summarizes the various phases that are observed in this study. In addition to the transitions between triangular and square lattices, other intermediate phases, such as the two-layered buckled (2B) phase as well as the $n\text{CL}\Delta$ phase characterized by a frozen contact layer in equilibrium with liquidlike inner layers, can be observed in the transition from n to $n + 1$ layers. The 2B phase, which has been observed in confined hard sphere systems,²¹ has, to our knowledge, not been identified in previous studies with confined soft spheres.

Since the fluid that is in equilibrium with the pore is a bulk liquid, the presence of solid phases at surface separations which accommodate one to six fluid layers indicates an elevation in the freezing point with respect to the bulk. In free energy simulations by Radhakrishnan et al., a general criterion for an elevation in the freezing temperature (relative to the bulk freezing point) was derived on the basis of the strength of the fluid–wall interaction.^{28,29} For strong fluid–wall interactions relative to fluid–fluid interactions, an elevation in the freezing point is expected. Soft sphere fluids confined in mica and graphitic pores fall into this category. Using a principle of corresponding states (valid for $\sigma_{\text{ff}}/\sigma_{\text{fw}}$ ratios close to unity, and sufficiently large reduced surface separations), the relative interaction strengths between fluid–wall relative to the fluid–fluid interaction was based on a dimensionless parameter, α . For strongly attractive pores, quantified by $\alpha > 1.15$, an elevation in the freezing temperature is predicted and free energy computations revealed the presence of a liquid phase, a frozen contact layer with liquidlike inner layers, and a crystalline phase as the temperature was lowered. For the OMCTS–mica potential used in this manuscript (eq 2), $\alpha = \rho_w \epsilon_{\text{fw}} \sigma_{\text{fw}}^2 / \epsilon_{\text{ff}} = 1.91$. The predicted elevation in freezing temperature as well as the presence of a frozen contact layer at larger pore widths is consistent with the global phase diagram predictions of Radhakrishnan et al.²⁸

4.2. Mica-K Surface. Our results show that including potassium ions on the mica surface disrupts the extended freezing and lattice transitions observed for the atomically smooth mica surface. The effect of potassium is akin to introducing atomic roughness to the mica surface and disrupts the formation of a frozen contact layer. However, the generic ability to form layers as the surface separation is increased is not disrupted. The ability of the inner layers to freeze by increasing in-plane order is dependent on the local density within the fluid layer. Hence, freezing of the inner layers is observed when the bulk activity is shifted to a point closer to the liquid–solid transition where the LJ parameters (Table 3) were adjusted to obtain the correct elevation from the freezing point of OMCTS. This counterintuitive situation where the contact layers are fluidlike with inner frozen layers presents a significant departure from the freezing scenarios reported for confined fluids. This result implies that freezing of the inner fluid layers does not necessarily require the presence of a frozen contact layer.

4.3. Comparison with Experiments. To our knowledge, this extended freezing behavior and the lattice transitions between Δ and \square lattices have not been documented for the specific set of interaction parameters corresponding to the OMCTS–mica system. Our study with the atomically smooth model for the mica surface (in the absence of potassium atoms) indicates that

the largest number of layers at which the first ordered structures are observed occurs when the pore accommodates six layers ($n = 6$). We point out that bulk state point A at which the GCMC simulations with the smooth mica surface were carried out corresponds to a bulk state point near the liquid–vapor coexistence curve, as illustrated in Figure 3. Liquid OMCTS at room temperature is about 5–10° above the melting point at 1 atm pressure and hence would lie in the region above the liquid–solid coexistence line in the phase diagram. The OMCTS Lennard-Jones parameters using the freezing point data and bulk density at room temperature yield point B in the bulk Lennard-Jones phase diagram (Figure 3). State point B lies at a temperature which is 6.5 K above the freezing point of bulk OMCTS;³² however, the liquid is now at a significantly higher pressure. Simulations carried out at this state point reveal a freezing behavior more extended than that reported above with state point A. Freezing was found to extend into the seven-layered regime, and the square-to-triangular transition persisted into the fourth layer ($n = 4$). The surface separations for which the frozen contact layer situations were observed occur over a broader range than with state point A.

Our results with the mica–K system are perhaps most representative of the experimental conditions. Freezing and solid–solid transitions observed with state point A and the atomically smooth mica surface are completely disrupted in the mica–K system. However, freezing of the inner layers is observed for $n \geq 3$ and persists (albeit weakly) into the seven-layered regime ($n = 7$), when the surfaces are equilibrated with state point B. The contact layer freezing scenario is no longer present in the mica–K system. This situation presents an interesting contrast with the results on an atomically smooth mica surface where the contact layers have a high degree of in-plane order. Notwithstanding the differences in the varying degree of crystallinity observed with the different surfaces and bulk state conditions investigated in this manuscript, our results clearly indicate that when in-plane ordering occurs, it happens over a single layer with decreasing surface separation. The increased in-plane order in the inner layers at $n = 7$ with the mica–K (state point B) system or at $n = 6$ (state point A) in the absence of potassium is likely to show signatures that are observed experimentally.³² In the mica–K system, the partly crystalline states suggest that the system is heterogeneous and would possess at least two relaxation times, one corresponding to the outer, more fluidlike contact layer and one corresponding to the inner, frozen system. Although partly crystalline, this would support the interpretation that the confined fluid exhibits a more glass-like behavior exhibited by multiple modes of relaxation within the framework of linear response.³⁴ However additional molecular dynamics simulations are required to pursue this issue.

In surface force experiments of the OMCTS–mica system, freezing, as inferred from the ability of the confined fluid to sustain a shear stress, is observed when six fluid layers are accommodated in the pore.³² The shear force data reveal a liquid-like response when the pore is able to accommodate seven or more layers, indicating that the transition from liquid (disordered) to solid (more ordered) occurs within the difference of a single layer. The transition between these two regimes was observed to be reversible within the time scale of the experiment, and solidification is inferred primarily by the reduction in the amplitude of lateral vibration of a spring attached in plane with the mica surface.

Although the experiments use the ability of the confined film to support a finite shear stress as a signature of solidification,

the modulus values are typically much lower than those of a bulk crystal, suggesting that the solid is a defective crystal,³¹ or “soft solid”. The looser packing of the inner atoms in our simulations at the larger surface separations where the pore fluid is completely frozen as well as the presence of frozen inner layers with a liquidlike outer layer in the mica–K system support this view. Equilibrium simulations carried out in an isostress–isostrain ensemble^{35,36} illustrate that confined fluid films (between atomically structured surfaces) that do not possess long range translational order (liquid-like) reveal rheological properties that are qualitatively similar to those of confined solids. The simulations show that layered fluids can show an initial elastic response to small amplitude shear, followed by the presence of a finite yield stress with increasing shear stress. This phenomenon is attributed to a local pinning of fluid atoms between the two surfaces.³⁵

Extrapolating from the work of Bock et al.,³⁶ all of the various fluid structure and layering scenarios present in this study are likely to show stress–strain characteristics qualitatively similar to those of a solid, and interpreting this alone as a signature of freezing (in the conventional sense) must be treated with caution. Barring the differences in the varying degrees of crystallinity observed in our equilibrium simulations, it is clear that confinement, in addition to layering, increases the in-plane order of the fluid and the number of layers at which this occurs is consistent (to within a single layer) with the experiment observation and interpretation of increased order with confinement.³²

To completely characterize the order in fluids confined to small nanometer separations, additional microscopy techniques which directly probe atomic order to augment the force and friction data are clearly required.^{36,50} Although surface force experiments can only indirectly infer the state of the pore fluid from a measured response, X-ray scattering methods³⁷ provide a more direct measurement of atomic order. X-ray scattering experiments of OMCTS confined between single crystal silicon surfaces suggest 2□ and 3□ packings for the confined molecules. These experiments are conducted at pressures in the MPa range. Although the surfaces are different, these experiments are in agreement with the square lattice symmetries observed in our study when $n = 2$ and 3. Before concluding this section, we note that, since OMCTS is in reality a quasispherical molecule, the influence and extent of its aspherical nature on the fluid structure upon confinement are yet to be fully assessed.⁵⁰

5. Summary and Conclusions

We have carried out GCMC simulations for a Lennard-Jones representation of OMCTS confined between two mica surfaces. Fluid structure is contrasted for both the atomically smooth mica surface as well as the mica surface containing potassium. It is now well-established that confined soft spheres can undergo a sequence of transitions between square and triangular lattices as the degree of confinement is varied. This change in lattice symmetry at a fixed number of confined layers is similar to that observed in confined colloidal suspensions. With the atomically smooth mica surface, inspection of the confined frozen phases reveals a wider sequence of structures than previously seen for confined soft spheres. In smaller surface separations where one to two fluid layers are accommodated, in addition to the square and triangular lattices found previously, the line buckled phase is also observed in surface separations where the transition from 1Δ to 2□ occurs. At larger surface separations of $n > 3$, prior to the admission of a new fluid layer, a frozen contact layer is found to coexist with liquidlike inner

layers. The OMCTS–mica system represents a strongly interacting confined system, and the extended freezing behavior as well as the presence of the frozen contact layer are qualitatively consistent with the global phase diagram predictions of freezing in atomically smooth walled nanopores by earlier workers.

Our results with the mica–K system present a significant departure from previously reported freezing scenarios under confinement. The small degree of roughness induced by the presence of potassium on the mica surface is sufficient to disrupt the presence of frozen phases and the sequence of solid–solid transitions observed as a function of surface separation with the atomically smooth mica surface. When simulations are carried out with a bulk state point in the proximity of the liquid–solid transition, an interesting counterintuitive freezing scenario is encountered with the mica–K system; the contact layers remain liquid-like, and inner fluid layers freeze with in-plane triangular symmetry.

This study and our earlier work on freezing in pores reveal that the variety of frozen phases that can occur in nanopores is extremely rich and the existence of frozen phases is governed by several factors. In the absence of epitaxial ordering driven by the lattice structure of the confining surface atoms, the fluid–wall interaction strength, degree of confinement, and bulk thermodynamic conditions play an important role. The bulk state point that is in equilibrium with the pore determines the pore density and the extent to which freezing can occur. The dependence on the bulk state point is expected to be weaker for strong fluid–wall interactions such as the OMCTS–mica system.

Although our broader interest lies in elucidating the extent of freezing as well as the symmetries of the possible frozen phases under confinement, the OMCTS–mica system enables comparison with results from surface force experiments. Our simulations carried out with and without the presence of potassium atoms on the mica surface with the bulk state point closer to the freezing line suggest that freezing of the pore fluid occurs in the range of six to seven fluid layers. This is in qualitative agreement with the situation observed experimentally. However, the confined fluid does not exist as a crystalline solid in the conventional sense and can consist of a disordered contact layer in contact with frozen inner layers. This situation negates the conventional view that ordering or crystallinity is greatest near the proximity of the surface and a frozen contact layer is needed for freezing to occur in the inner layers.

Acknowledgment. We would like to acknowledge the Department of Science and Technology India for financial support and Ateeque Malani for helpful discussions regarding the structure for the mica surface.

References and Notes

- (1) Snook, I. K.; van Megen, W. *J. Chem. Phys.* **1980**, *72*, 2907–2913.
- (2) Magda, J. J.; Tirrell, M.; Davis, H. T. *J. Chem. Phys.* **1985**, *83*, 1888–1901.
- (3) Gao, J.; Luedtke, W. D.; Landmann, U. *J. Phys. Chem. B* **1997**, *101*, 4013–4023.
- (4) Israelachvili, J. N. *Intermolecular and Surface Forces: with Applications to Colloidal and Biological Systems*; Academic: London, 1985.
- (5) Davis, H. T. *Statistical Mechanics of Phases, Interfaces and Thin Films*; VCH: New York, 1995.
- (6) Schoen, M.; Diestler, D. J.; Cushman, J. H. *J. Chem. Phys.* **1987**, *87*, 5464–5476.
- (7) Rhykerd, C. L., Jr.; Schoen, M.; Diestler, D. J.; Cushman, J. H. *Nature* **1987**, *330*, 461–463.
- (8) Bordarier, P.; Rousseau, B.; Fuchs, A. H. *Mol. Simul.* **1996**, *17*, 199–216.
- (9) Ayappa, K. G.; Ghatak, C. *J. Chem. Phys.* **2002**, *117*, 5373–5383.
- (10) Vishnyakov, A.; Neimark, A. V. *J. Chem. Phys.* **2003**, *118*, 7585–7598.
- (11) Salamacha, L.; Patrykiewicz, A.; Sokolowski, S.; Binder, K. *J. Chem. Phys.* **2004**, *120*, 1017–1030.
- (12) Pieranski, P.; Strzelecki, L.; Pansu, B. *Phys. Rev. Lett.* **1983**, *50*, 900–903.
- (13) van Winkle, D. H.; Murray, C. A. *Phys. Rev. A* **1986**, *34*, 562–573.
- (14) Murray, C. A.; Sprenger, W. O.; Wenk, R. A. *Phys. Rev. A* **1990**, *42*, 688–703.
- (15) Hug, J. E.; van Swol, F.; Zukoski, C. F. *Langmuir* **1995**, *11*, 111–118.
- (16) Schmidt, M.; Löwen, H. *Phys. Rev. Lett.* **1996**, *76*, 4552.
- (17) Schmidt, M.; Löwen, H. *Phys. Rev. E* **1997**, *55*, 7228–7241.
- (18) Marcus, A. H.; Rice, S. A. *Phys. Rev. E* **1996**, *55*, 637–656.
- (19) Zangi, R.; Rice, S. A. *Phys. Rev. E* **2000**, *61*, 660–670.
- (20) Nesper, S.; Bechinger, C.; Leiderer, P.; Palberg, T. *Phys. Rev. Lett.* **1997**, *79*, 2348–2351.
- (21) Fortini, A.; Dijkstra, M. *J. Phys.: Condens. Matter* **2006**, *18*, L371–L378.
- (22) Ghatak, C.; Ayappa, K. G. *Phys. Rev. E* **2001**, *64*, 051507.
- (23) Camara, L. G.; Bresme, F. *J. Chem. Phys.* **2004**, *120*, 11355–11358.
- (24) Salamacha, L.; Patrykiewicz, A.; Sokolowski, S.; Binder, K. *J. Chem. Phys.* **2005**, *122*, 074703.
- (25) Patrykiewicz, A.; Sokolowski, S. *J. Chem. Phys.* **2006**, *124*, 194705.
- (26) Nguyen, T. X.; Bhatia, S. K.; Nicholson, D. *J. Chem. Phys.* **2002**, *117*, 10827–10836.
- (27) Bock, H.; Gubbins, K. E.; Ayappa, K. G. *J. Chem. Phys.* **2005**, *122*, 094709.
- (28) Radhakrishnan, R.; Gubbins, K. E.; Sliwinska-Bartkowiak, M. *J. Chem. Phys.* **2000**, *112*, 11048–11057.
- (29) Radhakrishnan, R.; Gubbins, K. E.; Sliwinska-Bartkowiak, M. *J. Chem. Phys.* **2002**, *116*, 1147–1157.
- (30) Gelb, L. D.; Gubbins, K. E.; Radhakrishnan, R.; Sliwinska-Bartkowiak, M. *Rep. Prog. Phys.* **1999**, *62*, 1573–1659.
- (31) Alba-Simionesco, C.; Coasne, B.; Dosseh, G.; Dudziak, G.; Gubbins, K. E.; Radhakrishnan, R.; Sliwinska-Bartkowiak, M. *J. Phys.: Condens. Matter* **2006**, *18*, R15–R68.
- (32) Klein, J.; Kumacheva, E. *J. Chem. Phys.* **1998**, *108*, 6996–7009.
- (33) Kumacheva, E.; Klein, J. *J. Chem. Phys.* **1998**, *108*, 7010–7021.
- (34) Demirel, L. A.; Granick, S. *J. Chem. Phys.* **2001**, *115*, 1498–1512.
- (35) Schoen, M.; Hess, S.; Diestler, D. *J. Phys. Rev. E* **1995**, *52*, 2587–2602.
- (36) Bock, H.; Schoen, M. *J. Phys.: Condens. Matter* **2000**, *12*, 1545–1568.
- (37) Seeck, O. H.; Kim, H.; Lee, D. R.; Shu, D.; Kaendler, I. D.; Basu, J. K.; Sinha, S. K. *Europhys. Lett.* **2002**, *60*, 376–382.
- (38) Somers, S. A.; McCormick, A. V.; Davis, H. T. *J. Chem. Phys.* **1993**, *99*, 9890–9898.
- (39) Curry, J. E. *J. Chem. Phys.* **2000**, *113*, 2400–2406.
- (40) Curry, J. E. *Mol. Phys.* **2001**, *99*, 745–752.
- (41) Collins, D. R.; Catlow, C. R. *Am. Mineral.* **1992**, *77*, 1172.
- (42) Leng, Y.; Cummings, P. T. *Phys. Rev. Lett.* **2005**, *94*, 026101.
- (43) Cui, S. T.; Cummings, P. T.; Cochran, H. D. *J. Chem. Phys.* **2001**, *114*, 7189–7195.
- (44) Pashley, R. M. *J. Colloid Interface Sci.* **1981**, *83*, 531–546.
- (45) Jack, Y.; Josefowicz, J. K. A.; MacDiarmid, A. G. *Thin Solid Films* **2001**, *393*, 186–192.
- (46) Lee, S. H.; Rasaiah, J. C. *J. Phys. Chem.* **1996**, *100*, 1420.
- (47) Agarwal, R.; Kofke, D. A. *Mol. Phys.* **1995**, *85*, 43.
- (48) Johnson, K. J.; Zollweg, J. A.; Gubbins, K. E. *Mol. Phys.* **1993**, *78*, 591.
- (49) Allen, M. P.; Tildesley, D. J. *Computer Simulation of Liquids*; Clarendon Press: Oxford, U.K., 1987.
- (50) Granick, S.; Zhu, Y.; Lin, Z.; Bae, S.; Wong, J.; Turner, J. *Langmuir* **2006**, *22*, 2399–2401.
- (51) Su, Z.; Cushman, J. H.; Curry, J. E. *J. Chem. Phys.* **2003**, *118*, 1417–1422.
- (52) Lofti, A.; Vrabec, J.; Fischer, J. *Mol. Phys.* **1992**, *76*, 1319.
- (53) van Megen, W.; Snook, I. *J. Chem. Phys.* **1981**, *74*, 1409–1411.